Quantum Storage with Flat Bands

Carlo Danieli,[1] Jie Liu,[2] Rudolf A. Römer,[3,*] and Rodrigo A. Vicencio[4,5]
[1]Institute for Complex Systems, National Research Council (ISC-CNR), Via dei Taurini 19, 00185 Rome, Italy
[2]College of Electronic Information and Physics, Central South University of Forestry and Technology, Changsha 410004, China
[3]Department of Physics, University of Warwick, Gibbet Hill Road, Coventry CV4 7AL, United Kingdom
[4]Departamento de Física, Facultad de Ciencias Físicas y Matemáticas, Universidad de Chile, Santiago 8370448, Chile
[5]Millennium Institute for Research in Optics-MIRO, Santiago, Chile

(Received 1 August 2025; accepted 23 December 2025; published 10 February 2026)

The realization of robust quantum storage devices relies on the ability to generate long-lived, spatially localized states. In this Letter, we introduce a method for the targeted creation of compact excitations in flat-band lattices. By injecting *in-plane* radiation waves from the system's edge and applying a localized on-site potential at the desired storage position, we induce hybridization between compact localized states of the flat band and resonant dispersive plane waves. This hybridization enables the formation of spatially compact, stable excitations suitable for quantum memory applications. We experimentally validate this mechanism using photonic waveguide arrays, focusing on two representative geometries: the diamond chain and the one-dimensional Lieb ladder. Our approach is broadly applicable to any platform supporting flat-band physics.

DOI: 10.1103/7dfz-n1jh

Storage and retrieval of quantum states—also known collectively as "quantum memory" [1–5]—are key building blocks of novel quantum technology architectures, such as quantum computers [6–8], quantum communications [4,9–16], and the quantum internet [17,18]. Quantum memories use the quantum mechanical superposition principle to hold an exponentially growing number of states [19–21]. However, due to the noncloning theorem [22,23], the readout of such quantum memories remains a fundamental conceptual challenge. On the other hand, the storage of classical information using single quantum states is much more advanced. Since such systems do not use entanglement to store information, there is no need to clone the full quantum state, and only the projected information [24], i.e., whether the state was occupied or not, is enough to read the classical bit information. Even simpler quantum devices offer exciting potential for improvements over conventional storage devices [24,25]. For example, modern sub-15 nm, capacitor-based DRAM devices use 10 000–60 000 electrons to store a single bit [26,27], while using a single electronic state should, in principle, suffice. Of course, such an approach then runs into similar decoherence and instability issues as for qubits—unless one can find realizations of quantum states that are naturally stable and accessible.

In optical systems, such storage of light quanta (photons) has long been attempted. Kessel and Moiseev [28] discussed storage in a single photon state [29]. The experiment was demonstrated in 2003 [30]. Optical data storage can be achieved by using absorbers [31,32], e.g., different frequencies of light [33], which are then directed to beam space points and stored. Furthermore, light can be stored by conversion into an exciton, and the lifetime of the exciton can be enhanced by suitable engineering of the electron and hole separation [34–36], for example, in nanoring geometries [37].

The principal requirement of such single-state quantum storage devices is then to identify a system of similar states, which are numerous—to allow for storage of many classical bits—while also spatially local to allow ready access for readin and readout. Furthermore, we want systems with good stability to maximize the lifetime of these states. Flat-band (FB) lattices have many of these characteristics: they exhibit a macroscopically degenerate number of spatially compact eigenstates, that is, there are many of these states, and they are long-lived [38–41]. Experimentally, these locally compact flat-band states have been generated in a diverse range of systems, from atomic gases [42–44] to solid-state devices [45–48] and photonic lattices [49–51]. However, due to their degeneracy, the exact real-space location of the compact eigenstates to be excited has thus far been determined largely by chance when using nonlocal means.

In this Letter, we present a mechanism to selectively excite compactly localized states (CLSs) at desired positions in two

*Contact author: r.roemer@warwick.ac.uk

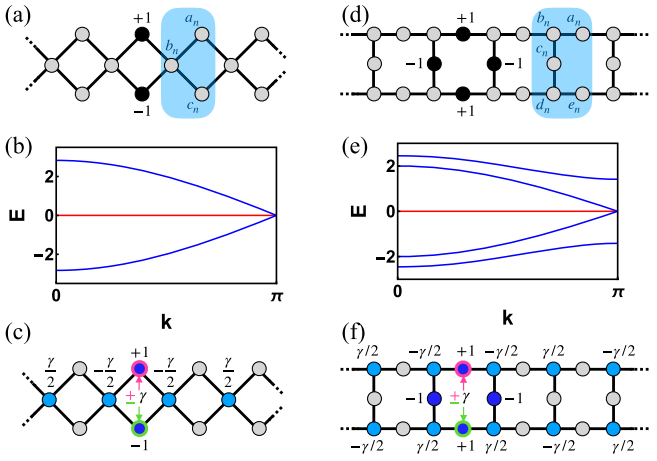

FIG. 1. (a) Schematic of the diamond chain. The three sites' unit cell is highlighted with the blue shaded area. The black circles show the position of the CLS with the corresponding amplitudes and phases as indicated. (b) Band structure of the diamond chain. The flat band is colored in red, while the two dispersive bands are colored in blue. (c) Hybridized state at $E = 0$. The blue circles indicate the location of the state with the corresponding amplitudes and phases as indicated. The on-site potentials are represented by the colored perimeters γ (magenta) and $-\gamma$ (green). (d)–(f) Similar diagrams as (a)–(c) for the Lieb ladder.

exemplary one-dimensional flat-band lattices: the diamond and the Lieb ladder. By shaping the local potential neighborhood, we guarantee the excitation of CLSs with the right phase structure. This aspect is particularly critical as, to the best of our knowledge, there is no simple way of exciting a FB compact state at an arbitrary position by nonlocal means. We experimentally implement this approach in a photonic setup and show quantitative agreement with our theoretical quantum storage mechanism. The fabricated lattices prove to be readily controllable via in-plane injection of light from the boundary for storage of classical bits at desired bulk plaquettes. The excitation method is based on a plane wave (PW) generator scheme that allows a selective excitation of specific radiation waves that resonate with the CLS at very precise regions.

Flat-band systems are usually studied in the language of electronic tight-binding lattices, and we shall follow this pathway here. For convenience, we study two paradigmatic models, namely, the so-called diamond chain and the quasi-1D Lieb ladder, as shown schematically in Figs. 1(a) and 1(d). In both lattices, the sites are arranged in plaquettes of $M = 4$ sites (for the diamond) and $M = 8$ sites (for the Lieb ladder), with constant hopping strength (equal to one for simplicity). Both models exhibit a flat band at $E = 0$, as detailed in Figs. 1(b) and 1(e), with the corresponding CLS given in Figs. 1(a) and 1(d). They also possess, respectively, additional $\nu - 1 = 2$ and $\nu - 1 = 4$ dispersive bands for a total of $\nu = 3$ and $\nu = 5$ Bloch bands [52]. We also note that these lattices are "chiral," that is, the lattices can be split in "majority" $\mathcal{M}$ and "minority" m sublattices with a different number of components [53,54]. For the diamond lattice, we have $\mathcal{M}_D = \{a_n, c_n\}_{n\in\mathbb{Z}}$ and $m_D = \{b_n\}_{n\in\mathbb{Z}}$, while for the Lieb ladder $\mathcal{M}_L = \{a_n, c_n, e_n\}_{n\in\mathbb{Z}}$ and $m_L = \{b_n, d_n\}_{n\in\mathbb{Z}}$. The CLS associated with the flat bands at $E = 0$ have profiles as shown in Figs. 1(a) and 1(d) by black dots, and they sit in the majority sublattices $\mathcal{M}_D$ and $\mathcal{M}_L$ in single plaquettes of both systems. For the diamond chain, the CLS form an orthogonal set of eigenstates as each one sits within a single unit cell, as shown in Fig. 1(a), and the flat-band energy can be shifted throughout the energy spectrum [55]. On the other hand, for the Lieb ladder, the CLSs form a nonorthogonal set of eigenstates with nontrivial overlap, as shown in Fig. 1(d), and the flat-band energy is fixed at $E = 0$ [38–41].

Flat-band eigenstates are degenerate at $E = 0$ for the lattices shown in Fig. 1. A traveling wave, resonant with the flat-band energy, will move across the lattice without exciting a preselected CLS location. A way to generate such a selection comes from observing in Figs. 1(b) and 1(e) that the flat bands touch the dispersive bands at $k = \pm\pi$. This implies that there exist extended zero-energy states $\mathcal{E}$, which are confined in the minority sublattices m_D and m_L of the networks—namely, $b_n = (-1)^n$ for the diamond chain and $b_n = (-1)^n$, $d_n = (-1)^{n+1}$ for the Lieb ladder. We then hybridize a number of target CLSs at unit cells $\mathcal{S} = \{n_j\}_{j=1}^{\mathcal{N}}$ with these $\mathcal{E}$ states by fine-tuning asymmetric on-site potentials at each n_j.

The tight-binding equations of motion of the lattices are

$$i\dot{\Psi}_n = \mathbf{H}_0\Psi_n + \mathbf{H}_1\Psi_{n+1} + \mathbf{H}_1^\dagger\Psi_{n-1} + \gamma\mathbf{V}\sum_{n_j\in\mathcal{S}}\Psi_{n_j}\delta_{n,n_j}, \quad (1)$$

where Ψ_n are complex vectors of ν components representing one unit cell. The matrices $\mathbf{H}_0$, $\mathbf{H}_1$, and $\mathbf{V}$ are $\nu\times\nu$ matrices such that $\mathbf{H}_0$ defines the unit-cell profile, and $\mathbf{H}_1$ the hopping between neighboring unit cells. For the diamond chain, we have

$$\mathbf{H}_0 = \begin{pmatrix} 0 & 1 & 0 \\ 1 & 0 & 1 \\ 0 & 1 & 0 \end{pmatrix}, \quad \mathbf{H}_1 = \begin{pmatrix} 0 & 1 & 0 \\ 0 & 0 & 0 \\ 0 & 1 & 0 \end{pmatrix}, \quad (2)$$

while for the Lieb ladder

$$\mathbf{H}_0 = \begin{pmatrix} 0 & 1 & 0 & 0 & 0 \\ 1 & 0 & 1 & 0 & 0 \\ 0 & 1 & 0 & 1 & 0 \\ 0 & 0 & 1 & 0 & 1 \\ 0 & 0 & 0 & 1 & 0 \end{pmatrix}, \text{ and } \mathbf{H}_1 = \begin{pmatrix} 0 & 1 & 0 & 0 & 0 \\ 0 & 0 & 0 & 0 & 0 \\ 0 & 0 & 0 & 0 & 0 \\ 0 & 0 & 0 & 0 & 0 \\ 0 & 0 & 0 & 1 & 0 \end{pmatrix}. \quad (3)$$

The matrix $\mathbf{V}$ defines the asymmetric potential localized within a unit cell n_j, while the parameter γ controls its

potential strength. In our lattices, the matrices respectively are

$$\mathbf{V}_{\mathrm{D}} = \begin{pmatrix} 1 & 0 & 0 \\ 0 & 0 & 0 \\ 0 & 0 & -1 \end{pmatrix}, \quad \mathbf{V}_{\mathrm{L}} = \begin{pmatrix} 1 & 0 & 0 & 0 & 0 \\ 0 & 0 & 0 & 0 & 0 \\ 0 & 0 & 0 & 0 & 0 \\ 0 & 0 & 0 & 0 & 0 \\ 0 & 0 & 0 & 0 & -1 \end{pmatrix}. \quad (4)$$

The asymmetric potentials are visually represented in Figs. 1(c) and 1(f) by magenta rings (for positive γ) and green rings (for negative γ). These local potentials modify the CLS at unit cell n_j, in both lattices, hybridizing them with the extended states $\mathcal{E}$. This results in defect eigenstates at $E = 0$, which we show in Figs. 1(c) and 1(f). In both panels, the dark blue sites in the perturbed plaquette have amplitudes equal to ± 1, while the light blue sites have amplitudes $\pm\gamma/2$. For weak potential strength $\gamma \ll 1$, such impurity states resemble the unperturbed CLS on top of an oscillating extended background. These potentials can be introduced independently in several target unit cells $\mathcal{S}$, yielding several defect states at $E = 0$.

The selection of one or more target CLSs can now proceed via excitation of the hybridized states using an *in-plane* incoming wave pulse. This is a novel mechanism that leverages these resonant defect states, and it applies in all platforms described via a tight-binding representation [Eq. (1)]. Furthermore, it supersedes the previous necessity of out-of-plane arrangements and precise modulation of the input beam [42–51]. We believe this to be an essential technical advancement for the engineering of future storage devices. In the following, we explore this mechanism both theoretically and experimentally using optical waveguide lattices, where the dynamical variable is the propagation coordinate z [56].

The defect states generated by the asymmetric potential in Eq. (4) are quasibound states in a continuum [57] that are not orthogonal to zero-energy dispersive waves. Therefore, they can be excited by launching an incoming pulse at $E = 0$ from an edge of the lattice. This demands the excitation of a PW at a tailored quasimomentum k_0 (in our cases, $k_0 = \pi$) with a Gaussian-like spatial envelope, which should be wide enough to have a narrow representation in momentum space around k_0. This concept, although being a standard technique in theoretical physics [58,59], is hard to realize in practice [60]. However, very recently [61] an experimental method to overcome this problem has been suggested, where the excitation of a side defect waveguide [62] yields the existence of an impurity state with a flat extended oscillating tail. The sharpness of the PW generator is strongly dependent on the coupling between the side defect and the respective lattice, but also on the specific geometry [63].

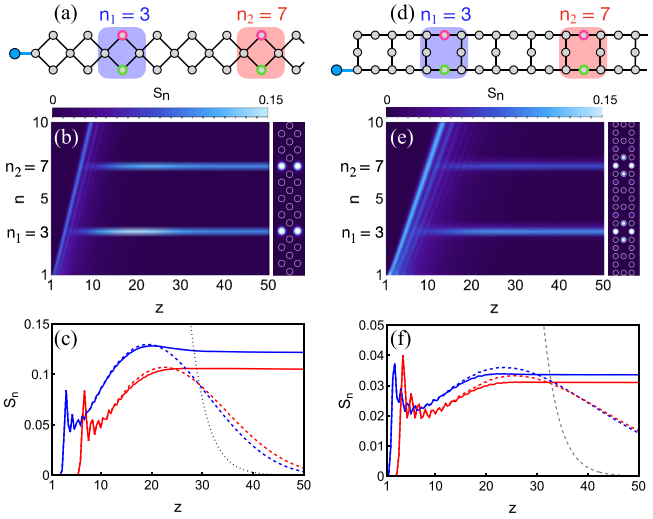

FIG. 2. (a) Eight plaquettes of the diamond chain. The two plaquettes with the on-site defects at $n = 3$ and $n = 7$ are highlighted with the blue and red shaded areas, respectively. The dark blue circle is the defect waveguide used to inject the wave packet around $E = 0$. (b) Intensity profile evolution S_n for an initial single-site excitation centred at the defect waveguide. The vertical right panel shows the local intensities $|\psi_n^j|^2$ at the final propagation distance. (c) Intensity evolution S_n for unit cells $n_1 = 3$ (blue) and $n_2 = 7$ (red). The solid lines are obtained with the sigmoid potential release applied, while the dashed curves are without. The black dotted curve indicates the sigmoid curve. (d)–(f) Similar diagrams to (a)–(c) for the Lieb ladder.

In our lattices, we realize the PW method by attaching a defect waveguide u in the left side of the lattices—guide colored in blue in Figs. 2(a) and 2(d). This means that in the first unit cell $n = 1$ of the diamond chain, the central site is governed by the equation $i\dot{b}_1 = a_1 + c_1 + Vu$ for a coupling strength V, while the equation of the defect waveguide is $i\dot{u} = Vb_1$, as shown in Fig. 2(a). In the Lieb ladder instead, we implement the same protocol by attaching the defect waveguide u to the bottom-left guide d of the unit cell, as shown in Fig. 2(d).

We numerically integrate the augmented lattice Eq. (1) for a single-site excitation in the defect waveguide $u(0) = 1$, $\Psi_n(0) = 0$, which introduces a radiating wave packet in the middle of the dispersive bands $E = 0$ for $k = \pi$ [64]. In our test, we perturb two unit cells $\mathcal{S} = \{3, 7\}$, as shown in Fig. 2 in blue and red shaded areas, respectively. Note that here we present simulations using relatively small system sizes (i.e., number of plaquettes) in order to compare with the experimental realization setup. Clearly, our results extend to lattices of hundreds of sites and several perturbed unit cells [63]. In Fig. 2(b) we show the light intensity in each unit cell $S_n(z)$ along the propagation distance z [65]. We turn off the impurities after the radiating pulse has passed by applying a sigmoid to the potential strength γ, i.e., the strength decays as $\gamma(z) = \gamma_0[1 - (1/1 + e^{-(z-z_0)/\tau})]$, with $\gamma_0 = 1/8$,

$z_0 = 20$, and $\tau = 2.5$ [66]. In Fig. 2(b), for $0 \leq z \lesssim 10$ we observe an initial ballistic traveling pulse generated by the defect waveguide. For $z \gtrsim 10$, after the PW front propagated beyond unit cell $n = 10$, the only nonvanishing local intensities S_n are at the perturbed unit cells $n = 3$ and $n = 7$. The vertical strip next to the propagation plot shows the output intensity profile. We observe that the light intensities are trapped only in the a and the c sites of the perturbed unit cells, analogously to the unperturbed CLS. Figure 2(c) clarifies this by showing the intensities S_n in the target unit cells $n = 3$ (blue) and $n = 7$ (red) with solid lines, which saturate at finite values. These results indicate that the light intensities that are trapped in the a and the c sites of the perturbed unit cells are not released since the connection with the lattice has been switched off via the sigmoid dependence. For comparison, in Fig. 2(c) we show with dashed lines that, for a constant $\gamma = 1/8$, the intensities S_n in the target unit cells 3 and 7 are decaying toward zero. Such a mechanism also occurs in the Lieb ladder, as shown in Figs. 2(d)–2(f). In this case, differently from the diamond chain, the CLSs form a nonorthogonal basis of the $E = 0$ flat band and the impurity state also is nonorthogonal to its neighboring CLS. Hence, exciting the impurity state via the local defect in Eq. (4) induces seemingly exponentially decaying excitations on neighboring plaquettes [67], as detailed in [63]. This additionally implies that (i) the amplitudes in the c sites, which induce the nonorthogonality, are less bright (weaker) than the a and e sites, as shown in Fig. 2(e), and (ii) the on-site potential should not be placed in adjacent unit cells, if a single-CLS readout is desired [63].

We fabricate several 1D photonic lattices by means of the femtosecond (fs) laser writing technique [68], as sketched in Fig. 3(a). A fs laser is tightly focused inside a borosilicate glass chip ($n_0 = 1.48$) and weakly modifies the refractive index contrast in the order of 10^{-4}–10^{-3} over n_0. The magnitude of the final change is determined by the fs laser power and the writing velocity in which the automatized translation stage moves in the propagation coordinate z. In this specific experiment, we fix the nominal fabrication power to $P_w = 20.5$ mW and the writing velocity to $v_w = 1.0$ mm/s. The asymmetric potential is experimentally inserted by modifying the velocity of the upper and lower sites at a specific plaquette. A linear and well-controlled dependence of the waveguides' propagation constants is achieved in our setup around the chosen v_w [63], where we simply take a faster (slower) writing velocity for deeper (shallower) waveguides. The propagation constant in the photonic implementation is directly equivalent to the site energy of tight-binding models [56,69], and to the potential strength γ.

All our experiments were performed on an $L = 50$ mm glass wafer, the maximum propagation length. However, we can effectively elongate this length by increasing the coupling constants through a wavelength-scan method [70,71].

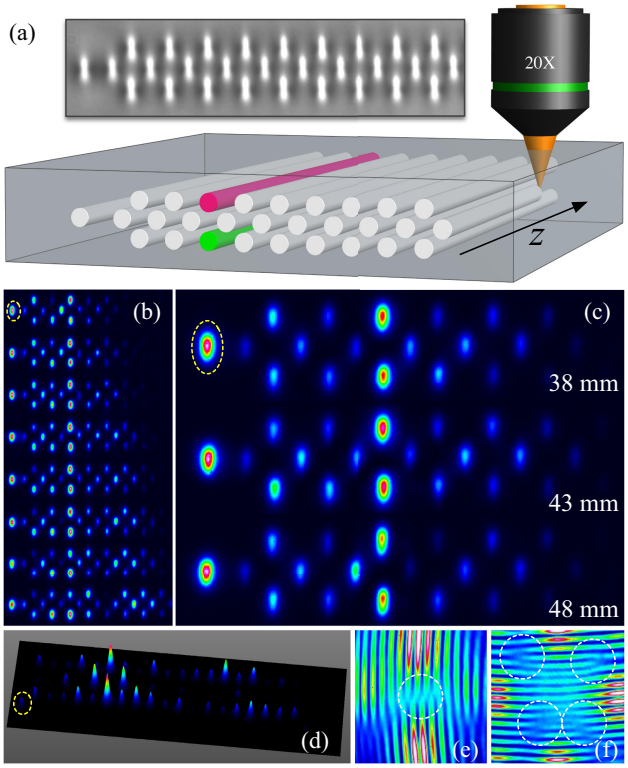

FIG. 3. (a) Sketch of the femtosecond laser writing technique describing the plane wave generator, a diamond lattice, and the asymmetric potential. The (top) inset shows a microscope image of a fabricated diamond lattice. (b),(c) Excitation of a FB localized state at the third ring of a diamond lattice for a λ scan in the interval $\{720, 790\}$ nm and for a z scan of the asymmetric potential at $\lambda = 745$ nm with z distance as given in mm for (c). (d) Excitation of a localized FB state at the third ring of a Lieb ladder at $\lambda = 765$ nm. (e),(f) Interferogram at $\lambda = 730$ nm for the excitation of diamond and Lieb ladders, respectively, with circles indicating the phase discontinuities. Yellow ellipses show the input position.

This allows us to adjust the effective propagation coordinate z, which in tight-binding-like models can be written as "Cz," with C the coupling constant (hopping). As larger wavelengths λ excite spatially wider guided modes, the coupling constants increase linearly with λ [72]. This means that a single lattice structure can be studied dynamically by ramping the wavelengths and by imaging the output intensity profiles. For example, Fig. 3(b) shows the effective evolution on a diamond lattice for a weak defect coupling, such that a significant part of the energy remains at the defect site. We observe how the excited wave packet propagates to the right and excites the FB state at the third plaquette. This figure shows very clearly the efficiency of our scheme, observing a quite perfect localized state even for larger wavelengths. After finding the optimal experimental conditions for the PW generator on diamond chains and Lieb ladders [63], we look for optimizing the switching off of the asymmetric potential, such to trap the FB localized state on a fully FB lattice.

Figure 3(c) shows an optimization for the asymmetric potential, at the indicated lengths for the diamond chain. We observe an optimal result for $z = 43$ mm, with a larger population of the FB state. These results confirm the numerical prediction using a sigmoid function for the inserted potential, so as to finally excite a pure FB lattice with a perfect FB out-of-phase profile.

We also performed several experiments on Lieb photonic ladders. The main challenge in this geometry is the increment of lattice sites and possible next-nearest-neighbor couplings [73,74], as well as the nonorthogonality of CLSs in this geometry. In addition, the natural waveguide ellipticity of the fabrication method [68] produces a strong asymmetry of vertical and horizontal coupling constants [63]. This produces a very asymmetric FB state, with essentially two main peaks at the top and bottom sites of the respective plaquette. After an intensive optimization process [63], we were able to excite a quite clear symmetric Lieb mode at the third plaquette, as shown in Fig. 3(d). In this case, the defect site is well coupled to the lattice and almost no energy remains at the excitation position. Finally, Figs. 3(e) and 3(f) show the interferograms at 730 nm for diamond and Lieb FB states, respectively. For diamond, we expect a FB state occupying the upper and bottom sites of a plaquette, with an out-of-phase configuration [70,75] [see Fig. 1(a)]. Figure 3(e) shows an out-of-phase pattern with a clear fringe discontinuity in between these two sites. For Lieb ladders [76], the FB state has four sites with a staggered phase structure [49,74,75] [see Fig. 1(d)]. This means that opposite sites are in phase, as we observe in Fig. 3(f) with a continuation of fringes. However, the staggered phase profile is expressed in the regions in between the four sites, observing in this figure clear fringe discontinuities, and a quite clear X-like phase profile.

In conclusion, our numerical and experimental results show that the notion of using CLSs as quantum storage devices is indeed possible. The ability of locally changing the environment to create an initial trap for the state to slot into can be seen as a local quantum "gate." Once sufficient intensity has accumulated in the indicated plaquette, the trap can be released, and the compactness of the FB states leads to a natural and perfect spatial confinement. The important conceptual advancement lies in the fact that the excitation of the state does not need to be done locally, but can rather be injected in-plane from the boundary of the device. This simplifies the engineering considerations considerably. Of course, a readout mechanism is also required. This is readily available by the same trap mechanism. Simply turning on the local gate leads to a release of the state as the perfect local resonance conditions no longer hold. The intensity then leaves the CLS and can be measured as a pulse intensity when leaving the system. While our demonstration has been done in photonic systems, the same principles hold for the full range of linear wave phenomena, from acoustics to electronics. In higher dimensions D, we found that this mechanism yields, in the 2D Lieb lattice, the excitation of extended-line states [77]. Still, compact excitations can be generated in 2D and 3D lattices by stacking, e.g., parallel diamond chains, where a single CLS can be excited in each line. The addition of external circuitry [78] could give extra degrees of freedom for a fully controllable and operational storage device. Last, one might want to speculate if the CLS mechanism can also support the concept of quantum memory based on entanglement as discussed above. When interactions—or nonlinearities—are carefully controlled, flat-band systems such as the 3D moire lattices might provide suitable hosts for such memories [79].

Acknowledgments—C. D., J. L., and R. A. R. thank the Center for Theoretical Physics of Complex Systems at the Institute for Basic Sciences, Daejoon, Korea, for generous hospitality in the initial stages of this work. C. D. acknowledges financial support from Project No. PNRR MUR PE 0000023-NQSTI and PNRR MUR Project No. CN 00000013-ICSC. J. L. gratefully acknowledges funding support from the General Project of Hunan Provincial Education Department, China (Grant No. 23C0102) and the Hunan Provincial Natural Science Foundation (Grant No. 2024JJ6708). R. A. V. acknowledges financial support from Millennium Science Initiative Program ICN17_012 and FONDECYT Grant No. 1231313.

Data availability—The data that support the findings of this article are openly available [80]; embargo periods may apply.

[1] C. Simon *et al.*, Eur. Phys. J. D **58**, 1 (2010).
[2] F. Bussières, N. Sangouard, M. Afzelius, H. de Riedmatten, C. Simon, and W. Tittel, J. Mod. Opt. **60**, 1519 (2013).
[3] E. Saglamyurek, N. Sinclair, J. Jin, J. A. Slater, D. Oblak, F. Bussières, M. George, R. Ricken, W. Sohler, and W. Tittel, Nature (London) **469**, 512 (2011).
[4] M.-H. Jiang, W. Xue, Q. He, Y.-Y. An, X. Zheng, W.-J. Xu, Y.-B. Xie, Y. Lu, S. Zhu, and X.-S. Ma, Nat. Commun. **14**, 6995 (2023).
[5] A. I. Lvovsky, B. C. Sanders, and W. Tittel, Nat. Photonics **3**, 706 (2009).
[6] P. Nimbe, B. A. Weyori and A. F. Adekoya, Quantum Inf. Process. **20**, 80 (2021).
[7] S. S. Gill *et al.*, *Quantum Computing Principles and Paradigms* (Elsevier, New York, 2025).
[8] Q. A. Memon, M. Al Ahmad, and M. Pecht, Quantum Rep. **6**, 627 (2024).
[9] A. G. Radnaev, Y. O. Dudin, R. Zhao, H. H. Jen, S. D. Jenkins, A. Kuzmich, and T. A. B. Kennedy, Nat. Phys. **6**, 894 (2010).
[10] A. Wallucks, I. Marinković, B. Hensen, R. Stockill, and S. Gröblacher, Nat. Phys. **16**, 772 (2020).

[11] S. Ritter, C. Nölleke, C. Hahn, A. Reiserer, A. Neuzner, M. Uphoff, M. Mücke, E. Figueroa, J. Bochmann, and G. Rempe, Nature (London) **484**, 195 (2012).

[12] J. Hofmann, M. Krug, N. Ortegel, L. Gérard, M. Weber, W. Rosenfeld, and H. Weinfurter, Science **337**, 72 (2012).

[13] Y. Yu, F. Ma, X.-Y. Luo, B. Jing, P.-F. Sun, R.-Z. Fang, C.-W. Yang, H. Liu, M.-Y. Zheng, X.-P. Xie, W.-J. Zhang, L.-X. You, Z. Wang, T.-Y. Chen, Q. Zhang, X.-H. Bao, and J.-W. Pan, Nature (London) **578**, 240 (2020).

[14] I. Usmani, C. Clausen, F. Bussières, N. Sangouard, M. Afzelius, and N. Gisin, Nat. Photonics **6**, 234 (2012).

[15] D. L. Moehring, P. Maunz, S. Olmschenk, K. C. Younge, D. N. Matsukevich, L.-M. Duan, and C. Monroe, Nature (London) **449**, 68 (2007).

[16] Y.-F. Pu, S. Zhang, Y.-K. Wu, N. Jiang, W. Chang, C. Li, and L.-M. Duan, Nat. Photonics **15**, 374 (2021).

[17] S. Wehner, D. Elkouss, and R. Hanson, Science **362**, eaam9288 (2018).

[18] H. J. Kimble, Nature (London) **453**, 1023 (2008).

[19] H. Bernien, B. Hensen, W. Pfaff, G. Koolstra, M. S. Blok, L. Robledo, T. H. Taminiau, M. Markham, D. J. Twitchen, L. Childress, and R. Hanson, Nature (London) **497**, 86 (2013).

[20] P. C. Humphreys, N. Kalb, J. P. J. Morits, R. N. Schouten, R. F. L. Vermeulen, D. J. Twitchen, M. Markham, and R. Hanson, Nature (London) **558**, 268 (2018).

[21] C.-W. Chou, J. Laurat, H. Deng, K. S. Choi, H. de Riedmatten, D. Felinto, and H. J. Kimble, Science **316**, 1316 (2007).

[22] W. K. Wootters and W. H. Zurek, Nature (London) **299**, 802 (1982).

[23] D. Dieks, Phys. Lett. **92A**, 271 (1982).

[24] M. Röntgen, C. V. Morfonios, I. Brouzos, F. K. Diakonos, and P. Schmelcher, Phys. Rev. Lett. **123**, 080504 (2019).

[25] H. Li, R. Huang, R. Dong, S. Li, H. Huang, X. Zhang, Z. Chen, P. Zhan, and Z. Wang, Phys. Rev. Appl. **23**, 054027 (2025).

[26] Micron D1 α, the most advanced node yet on DRAM, https://semiengineering.com/micron-d1%CE%B1-the-most-advanced-node-yet-on-dram/.

[27] *Micro and Nanoelectronics Devices, Circuits and Systems: Select Proceedings of MNDCS 2022*, edited by T. R. Lenka, D. Misra, and L. Fu (Springer, New York, 2023), p. 528.

[28] A. R. Kessel and S. A. Moiseev, JETP Lett. **58**, 81 (1993), http://jetpletters.ru/ps/0/article_18171.shtml.

[29] R. K. Mohan, B. Luo, S. Kröll, and A. Mair, Phys. Rev. A **58**, 4348 (1998).

[30] N. Ohlsson, S. Kröll, and S. A. Moiseev, in *Coherence and Quantum Optics VIII* (Springer, Boston, MA, 2003), pp. 383–384.

[31] N. Landy and D. Smith, Nat. Mater. **12**, 25 (2013).

[32] N. J. Turro, in *Applied Photochemistry* (Springer, Berlin, Heidelberg, 2009), pp. 201–230.

[33] B. A. Munk, *Frequency Selective Surfaces: Theory and Design* (John Wiley & Sons, New York, 2000).

[34] R. A. Römer and M. E. Raikh, Phys. Rev. B **62**, 7045 (2000).

[35] A. M. Fischer, V. L. Campo, M. E. Portnoi, and R. A. Römer, Phys. Rev. Lett. **102**, 096405 (2009).

[36] M. D. Teodoro, V. L. Campo, V. Lopez-Richard, E. Marega, G. E. Marques, Y. G. a. Gobato, F. Iikawa, M. J. S. P. Brasil, Z. Y. AbuWaar, V. G. Dorogan, Y. I. Mazur, M. Benamara, and G. J. Salamo, Phys. Rev. Lett. **104**, 086401 (2010).

[37] V. Fomin, *Physics of Quantum Rings*, 2nd ed., NanoScience and Technology (Springer International Publishing, Cham, 2018).

[38] D. Leykam, A. Andreanov, and S. Flach, Adv. Phys. X **3**, 677 (2018).

[39] D. Leykam and S. Flach, APL Photonics **3**, 70901 (2018).

[40] R. A. Vicencio Poblete, Adv. Phys. X **6**, 1878057 (2021).

[41] C. Danieli, A. Andreanov, D. Leykam, and S. Flach, Nanophotonics **13**, 3925 (2024).

[42] R. Shen, L. B. Shao, B. Wang, and D. Y. Xing, Phys. Rev. B **81**, 041410(R) (2010).

[43] V. Apaja, M. Hyrkäs, and M. Manninen, Phys. Rev. A **82**, 041402(R) (2010).

[44] S. Taie, H. Ozawa, T. Ichinose, T. Nishio, S. Nakajima, and Y. Takahashi, Sci. Adv. **1**, e1500854 (2015).

[45] J. Vidal, R. Mosseri, and B. Douçot, Phys. Rev. Lett. **81**, 5888 (1998).

[46] C. C. Abilio, P. Butaud, T. Fournier, B. Pannetier, J. Vidal, S. Tedesco, and B. Dalzotto, Phys. Rev. Lett. **83**, 5102 (1999).

[47] R. Drost, T. Ojanen, A. Harju, and P. Liljeroth, Nat. Phys. **13**, 668 (2017).

[48] M. R. Slot, T. S. Gardenier, P. H. Jacobse, G. C. Van Miert, S. N. Kempkes, S. J. Zevenhuizen, C. M. Smith, D. Vanmaekelbergh, and I. Swart, Nat. Phys. **13**, 672 (2017).

[49] R. A. Vicencio, C. Cantillano, L. Morales-Inostroza, B. Real, C. Mejía-Cortés, S. Weimann, A. Szameit, and M. I. Molina, Phys. Rev. Lett. **114**, 245503 (2015).

[50] S. Mukherjee, A. Spracklen, D. Choudhury, N. Goldman, P. Öhberg, E. Andersson, and R. R. Thomson, Phys. Rev. Lett. **114**, 245504 (2015).

[51] S. Xia, Y. Hu, D. Song, Y. Zong, L. Tang, and Z. Chen, Opt. Lett. **41**, 1435 (2016).

[52] The dispersive bands of the diamond chain are $E^d_{2,3}(k) = \pm 2\sqrt{2}\cos(k/2)$, while in the Lieb case the two dispersive bands $E^l_{2,3} = \pm\sqrt{2+2\cos k}$ of the diamond are paired up with $E^l_{4,5}(k) = \pm\sqrt{4+2\cos k}$.

[53] A. Ramachandran, A. Andreanov, and S. Flach, Phys. Rev. B **96**, 161104(R) (2017).

[54] D. Călugăru, A. Chew, L. Elcoro, Y. Xu, N. Regnault, Z.-D. Song, and B. A. Bernevig, Nat. Phys. **18**, 185 (2022).

[55] S. Flach, D. Leykam, J. D. Bodyfelt, P. Matthies, and A. S. Desyatnikov, Europhys. Lett. **105**, 30001 (2014).

[56] F. Lederer, G. I. Stegeman, D. N. Christodoulides, G. Assanto, M. Segev, and Y. Silberberg, Phys. Rep. **463**, 1 (2008).

[57] A. R. Legón, M. Ahumada, J. P. Ramos-Andrade, R. A. Molina, and P. A. Orellana, Phys. Rev. A **111**, 013529 (2025).

[58] R. A. Vicencio, J. Brand, and S. Flach, Phys. Rev. Lett. **98**, 184102 (2007).

[59] R. A. Vicencio, A. V. Gorbach, and S. Flach, Phys. Lett. A **354**, 210 (2006).

[60] C. Cantillano, L. Morales-Inostroza, B. Real, S. Rojas-Rojas, A. Delgado, A. Szameit, and R. A. Vicencio, Sci. Bull. **62**, 339 (2017).

[61] B. Real, D. Guzmán-Silva, and R. A. Vicencio, Phys. Rev. B **109**, 064308 (2024).

[62] A. Tetarwal, S. Sharma, and S. Mukherjee, Opt. Lett. **50**, 4626 (2025).
[63] See Supplemental Material at http://link.aps.org/supplemental/10.1103/7dfz-n1jh for simulations of larger systems, waveguides fabrication, numerical calibration of PW generators, and experimental optimization of Diamond and Lieb ladders.
[64] Note that radiating wave packet in different part of the dispersive bands can be achieved by introducing an on-site potential β_u in the defect waveguide, i.e., rendering its equation $i\dot{u} = \beta_u u + V_u b_1$ [61].
[65] In the diamond chain $S_n(z) = |a_n(z)|^2 + |b_n(z)|^2 + |c_n(z)|^2$, while for the Lieb ladder $S_n(z) = |a_n(z)|^2 + |b_n(z)|^2 + |c_n(z)|^2 + |d_n(z)|^2 + |e_n(z)|^2$.
[66] These parameters have been obtained via systematic scanning of the parameters γ, z_0, and τ. The values used in our simulations to capture CLS states are not unique. However, these are the resulting values that yielded the clearest captures of the CLS state.
[67] J. T. Chalker, T. S. Pickles, and P. Shukla, Phys. Rev. B **82**, 104209 (2010).
[68] A. Szameit, D. Blömer, J. Burghoff, T. Schreiber, T. Pertsch, S. Nolte, A. Tünnermann, and F. Lederer, Opt. Express **13**, 10552 (2005).
[69] D. Guzmán-Silva, G. Cáceres-Aravena, and R. A. Vicencio, Phys. Rev. Lett. **127**, 066601 (2021).
[70] G. Cáceres-Aravena, B. Real, D. Guzmán-Silva, P. Vildoso, I. Salinas, A. Amo, T. Ozawa, and R. A. Vicencio, APL Photonics **8**, 080801 (2023).
[71] G. Cáceres-Aravena, M. Nedić, P. Vildoso, G. Gligorić, J. Petrovic, A. Maluckov, and R. A. Vicencio, Phys. Rev. Lett. **133**, 116304 (2024).
[72] R. A. Vicencio, F. G. L. Cárcamo-Macaya, D. Román-Cortés, and P. Solano, Phys. Rev. Lett. **135**, 013601 (2025).
[73] D. Leykam, O. Bahat-Treidel, and A. S. Desyatnikov, Phys. Rev. A **86**, 031805(R) (2012).
[74] L. Morales-Inostroza and R. A. Vicencio, Phys. Rev. A **94**, 043831 (2016).
[75] S. Mukherjee and R. R. Thomson, Opt. Lett. **40**, 5443 (2015).
[76] D. Román-Cortés, G. Fadic, C. Cid-Lara, D. Guzmán-Silva, B. Real, and R. A. Vicencio, Sci. Rep. **11**, 21411 (2021).
[77] S. Xia, A. Ramachandran, S. Xia, D. Li, X. Liu, L. Tang, Y. Hu, D. Song, J. Xu, D. Leykam, S. Flach, and Z. Chen, Phys. Rev. Lett. **121**, 263902 (2018).
[78] Y.-J. Chang, Y.-H. Lu, Y. Wang, X.-Y. Xu, W.-H. Zhou, W.-H. Cui, X.-W. Wang, J. Gao, L.-F. Qiao, and X.-M. Jin, Phys. Rev. Lett. **126**, 110501 (2021).
[79] Z. Gao, V. V. Konotop, R. Peng, Z. Xu, Z. Yang, and F. Ye, Nat. Commun. **16**, 6306 (2025).
[80] C. Danieli, J. Liu, R. A. Römer, and R. A. Vicencio, Warwick Research Archive Portal, https://wrap.warwick.ac.uk/192293/ (2026).